JP3J.24 THE DEVELOPMENT AND STRUCTURE OF AN OCEANIC SQUALL LINE SYSTEM DURING THE SOUTH CHINA SEA MONSOON EXPERIMENT

Jian-Jian Wang[1,2], Lawrence Carey[3]
[1]Goddard Center for Earth Science and Technology, University of Maryland Baltimore County
[2]Mesoscale Atmospheric Processes Branch, NASA/GSFC
[3]Department of Atmospheric Sciences, Texas A & M University

1. INTRODUCTION

The evolution and structure of convection in the tropics are of considerable interest because it lies at the heart of heat, moisture and momentum fluxes. Characterization of the vertical structure of tropical convection is a major objective of the Tropical Rainfall Measuring Mission (TRMM) launched by National Aeronautics and Space Administration (NASA) (Simpson et al., 1988). To support TRMM, a series of field campaigns were conducted in various tropical locations in order to provide detailed information on tropical convection. The South China Sea Monsoon Experiment (SCSMEX), conducted in the South China Sea (SCS) and surrounding area in 1998, aimed at a better understanding of the key physical processes for the onset, maintenance and variability of the monsoon over Southeast Asia and southern China leading to improved monsoon predictions (Lau et al. 2000, Tao et al. 2003). The SCSMEX also served as one of the TRMM experiments that was designed to study the precipitation and kinematic structures of mesoscale convection in an oceanic environment.

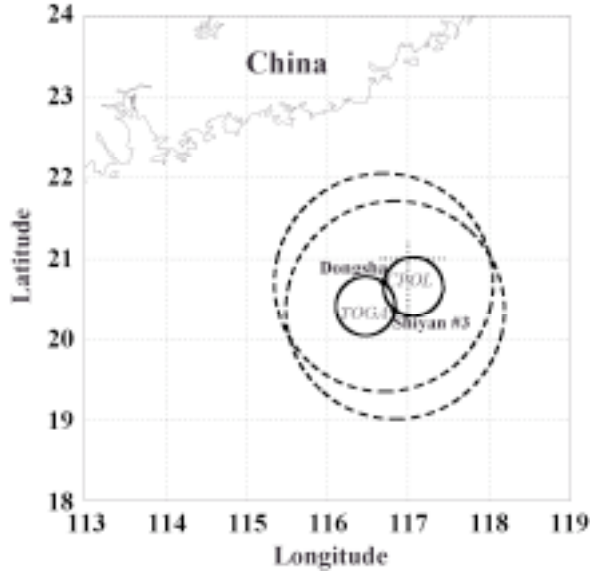

Fig. 1 Dual-Doppler radar network during SCSMEX. The big circles indicate the radar observing domain, while the small circles show the dual-Doppler radar analysis regime.

The main objective of the mesoscale program of the SCSMEX is to define the initiation, structure, evolution and dynamics of precipitation systems associated with the onset and mature phase of the SCS summer monsoon. In this study, we will perform a detailed study of the evolution and structure of a squall line system that was observed for the first time in the SCS region during the summer monsoon season.

2. THE EVOLUTION OF THE SQUALL-LINE

The squall line system including several lines persisted from 1200 UTC 24 May to 0500 UTC 25 May. The early convective echoes appeared at about 1200 UTC as several individual newly formed convective cells. The cells to the south were relatively intense with maximum radar reflectivity reaching 40 dBZ. These small cells lined up in a discontinuous arc-shaped convective line about 50 km west of the C-POL radar (Fig. 2a). The north-south orientation of the convective line is perpendicular to the low-level wind shear (1000 to 800 hPa). This was consistent with the studies on western Pacific convection by LeMone et al. (1998) who found the orientation of the convection tends to be perpendicular to the low-level (surface to 800 hPa) wind shear if its magnitude is over 4 m s^{-1}. While moving eastward, this convective line gradually intensified into a broader, stronger, and more organized squall line. This squall line reached its climax both in size and intensity near 1600 UTC. The peak reflectivity of 50 dBZ was recorded at 3 km MSL with the echo top at 12 km MSL. The squall line started to dissipate after 1600 UTC.

Along with the decay of the first squall line, a new and intense convective line started to develop about 40 km behind the original squall line (Fig. 2b). Compared to the echoes in the first squall line, the main echo of the second squall line at its early stage was more intense with larger area coverage. At 2200 UTC, the second squall line was at its mature stage showing a continuous convective band with the east-west extension up to 50 km. The peak radar reflectivity of about 55 dBZ was recorded at 1.5-3.0 km MSL. Overall, the second squall line was larger and more intense than the first squall line. With the echo top reaching 15 km MSL, the second squall line was also the tallest convection observed on 24 May.

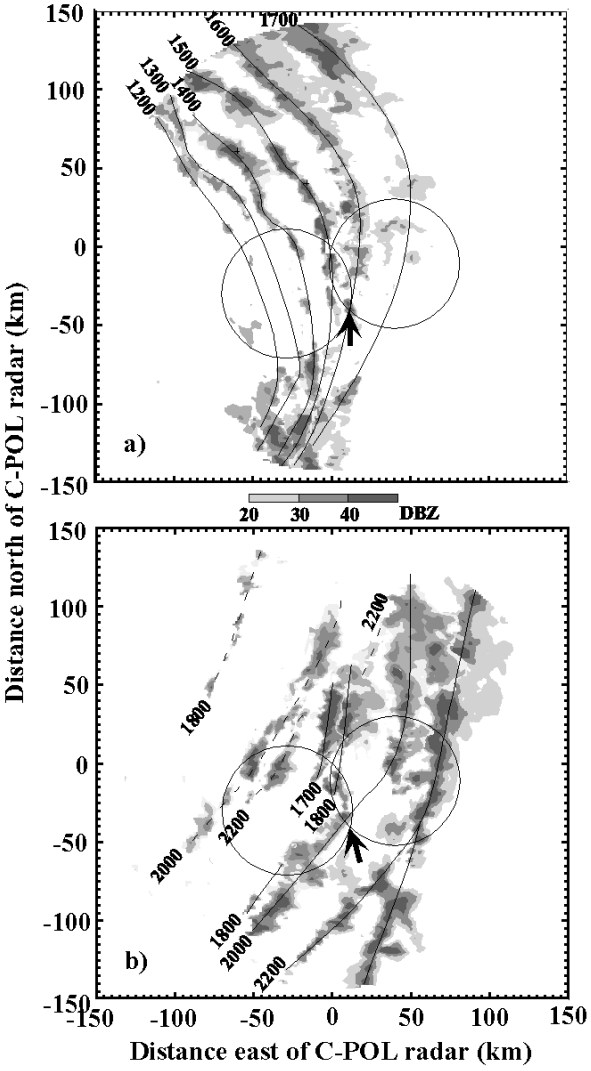

Fig. 2 Time series of the C-POL radar reflectivity (dBZ) at 2.5 km MSL for the evolution of the main echoes of (a) the first squall line, and (b) the second (solid line) and third (dashed line) squall lines on 24 May.

About an hour later after the formation of the second squall line, to the northwest, several new cells developed and lined up in a northeast to southwest direction about 80 km behind the second squall line at 1800 UTC. These cells formed a more continuous convective line later and became the third squall line observed on 24 May. However, after 2200 UTC when the second squall line was at its mature phase, the third squall line to the west weakened to a short line and dissipated in the next hour or so. In contrast to the second squall line, the third squall line did not become a well-organized line with significant intensity before its dissipation. Without enough data around the third line or between the second and third line, we are not sure about the cause for the dissipation of the third line. However, considering that the third line was just a few tens of kilometers behind the mature and intense second line, we believe that the effects of the second line may have played a role in this process. For instance, the mesoscale descending motion often detected after the passage of strong convection may suppress the maintenance of updrafts and result in the weakening of the third line.

3. RAINFALL AND KINEMATIC STRUCTURE

In this section, the precipitation and kinematic structure of the squall lines will be discussed. More attention will be paid to the second squall line, the most intense and well-organized one. During its mature phase, the second squall line was located in the dual-Doppler radar analysis lobes, which is good for a detailed study of its kinematic structure.

The vertical cross sections of radar reflectivity, differential reflectivity, system-relative wind, and vertical velocity across the two principal cells are shown in Fig. 3. The echo top reached 14-16 km MSL. Although not shown in our interpolation, the actual maximum radar reflectivity recorded was about 55 dBZ. An important characteristic of this squall line, also discussed earlier with horizontal cross-sections, was that the front to rear low-level inflow extended all the way to the very rear part of the cell. The deceleration of the low-level inflow from the front portion was also evident. In the southern cell (Fig. 3c), the formation of a new cell behind the old cell was apparent. The low-level maximum updraft was also located in the convection zone at the rear of the system (Figs. 3b and 3d). This type of strong updraft at the rear also implied that the inflow must pass a region ahead of the convective line before entering the convective tower. Theoretically, this type of structure may have some negative effects on the development and maintenance of the deep convection. When the inflow passes through the convective precipitating area, it could be chilled by the cool air caused by evaporative cooling. As a result, the buoyancy of the air in the updraft might be reduced. Consequently, the intensity of the updraft and the convection might weaken as well. Nevertheless, from a simple 2-D numerical simulation, Parker (2002) argued that the evaporative cooling actually occurs over a relatively deep layer with cooling increasing with height over the lowest 2-2.5 km. Therefore, the net effects of this process is to further destabilize the low levels and result in an increased CAPE. The maximum updraft was about 5-7 m s^{-1} at an elevated height of 9-10 km MSL (Figs. 3b and 3d). Downdrafts were located just ahead of the updrafts.

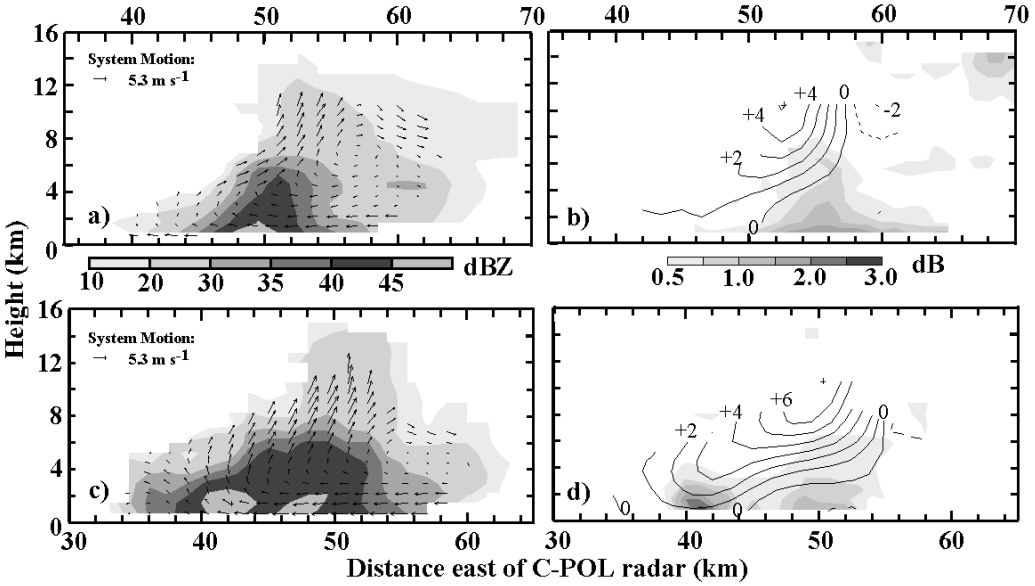

Fig. 3 Vertical cross section of (a) Radar reflectivity (dBZ) and system-relative wind flow, and (b) vertical air motion (m s^{-1}, contoured) and differential reflectivity (dB, shaded) for a developing cell valid at 2040 UTC. (c) and (d) are same as (a) and (b), respectively, but for a mature cell.

Consistent with the weaker updrafts in a tropical oceanic environment, there was a sharp reflectivity gradient above the 0°C level.

Despite radar reflectivity over 50 dBZ, both the first and second squall line had little stratiform precipitation accompanying the convective portion. Using a partitioning algorithm based on Steiner et al. (1995), we found that the stratiform area on 24 May accounted for only 10-15% of the total rain area. This was far less than the overall 63-70% stratiform occurrence during four TRMM field experiments in the tropics (Tokay et al., 2001). The environmental soundings clearly showed that the mid- to upper-level air was quite dry. As determined from modeling studies by W.-K. Tao (NASA/GSFC, personal communication), the dry air in the mid- to upper-levels generally results in a rapid evaporation of the stratiform cloud after the passage of its convective counterpart. The effects of dry air aloft on the stratiform rain development are more significant in the tropical oceanic region than in a mid-latitude continental environment. In a mid-latitude continental circumstance, the convective induced updrafts could be much stronger than that in a tropical oceanic area. Therefore, the deleterious microphysical effects of evaporation in a dry environment may be overcome by the convectively driven mesoscale circulation. With enough low-level moisture and buoyancy, the pronounced updrafts may advect hydrometeors to moisten the dry environment and result in the formation of stratiform rain. As a result, extensive stratiform regions may be observed in an environment with dry mid-to-upper layers (e.g. Houze 1993). However, for the tropical squall line case studied here, the vertical velocities at the cloud base (1-2 m s^{-1}) were weak and the buoyancy was limited. Both of these factors prevented the system from generating stratiform regions. In addition, the weak system-relative upper-level winds may also play a role in minimizing the scale of stratiform rain by failing to advect hydrometers away from the convective cores. In fact, there was no long lasting stratiform rain with considerable area coverage on 24 May.

The only signs of stratiform rain formation could be found in the vertical cross section across the intense northern cell (Fig. 3a). There was a nose of weak reflectivity area at around 8 km MSL ahead of the leading edge of the squall line. A forward tilt of roughly 40° from the horizontal was seen in both the vertical airflow and reflectivity contours in the cross section. The forward tilt of radar reflectivity indicated the tendency of stratiform rain ahead of the system. There was also a small local reflectivity maxima at about 4.5 km just below the eastward leaning reflectivity contour. This mid-level reflectivity maximum, or radar bright band, was a clear sign of stratiform rain and marked the position of the melting layer. From most previous observational (LeMone et al 1984, Jorgensen et al. 1997) and modeling (Trier et al. 1996, 1997) studies, it was found that a rearward tilting

of the inflow was more common and usually resulted in a stratiform region trailing the convective part. Rotunno et al. (1988) illustrated the important role of the cold pool in shaping the structure of the squall line by balancing the horizontal vorticity of the low-level shear. When a cold pool dominates the circulation, the circulation progressively leans further upshear, i.e., forming a trailing stratiform region. On the other hand, in the presence of a weak cold pool, an updraft/thermal will tilt downshear, i.e., forming a leading stratiform region. In other words, if the horizontal vorticity associated with the cold pool resulting from evaporation is insufficient to counteract the circulation driven by lower-tropospheric vertical shear the downshear tilt of the convection and the leading stratiform region would form. Although the lack of the in-situ thermodynamic measurements in this study makes it difficult to determine an accurate intensity of the cold pool, an analysis of the environmental soundings (not shown) may provide a reasonable estimation of the contribution from evaporative cooling in downdrafts. Usually, the downdraft originates near the level of minimum wet-bulb potential temperature about 3-5 km above the ground. The downdraft path assuming sufficient rainwater to maintain saturation for the entire descent can be estimated by following the moist adiabatic processes, i.e., wet-bulb potential temperature curve on a thermodynamic diagram, to the surface. The maximum cooling is the temperature difference between the downdraft air and the environmental air at the surface. However, if the air descends subsaturated, the parcel temperature will be greater than its wet-bulb temperature and the cooling will be less. For the present case, the possible maximum cooling was only about 4-5°C. This suggested that a downdraft produced cold pool with sufficient strength to produce an upshear tilted convection was unlikely.

Another difference of the current case from the previous observations (Roux 1988; Jorgensen 1997) and simulations (Trier et al. 1997; Robe and Emmanuel 2001) of tropical squall lines was the lack of a pronounced environmental low-level jet. The absence of the low-level jet removed the reverse shear above the jet that may support the rearward advection of warm and moist air above the cold pool. That rearward advection discussed in previous literature may further strengthen the vertical distribution of buoyancy associated with midlevel convergence and upper-tropospheric ascent, and therefore help the development of stratiform rain in the trailing regions (Houze 1993). In a climatological study, Parker and Johnson (2000) found that the trailing or paralleling stratiform rain occurs in over 80% of convective lines observed in the mid-latitudes over the United States, while the leading stratiform cases only account for 19%. However, combining the analysis in this study and the previous SCSMEX study by Wang (2004), leading stratiform mode convection seems very common during the onset period of the SCS summer monsoon.

3. HYDROMETEOR CHARACTERISTICS

Cross-sections of Z_{DR} for the intense cells sampled at 2040 UTC are also shown in Figs. 3b and 3d. In general, Z_{DR} columns were constrained to relatively low levels. The contour of 1 dB was found in the lowest 3 km, well below the 0°C level. This indicated that oblate drops with diameter over 1.5 mm only existed in the lower levels and were not lofted into the mixed phase region. Our results shown here had some similarity to the TRMM-LBA westerly case (Cifelli et al. 2002), However, the raindrops were less oblate (and hence smaller) and limited to even lower levels. For the convective cells at their mature phase (northern cell in Fig. 3b and east of the southern cell in Fig. 3d), the mid-sized raindrops indicated by Z_{DR} of 0.5-1.0 dB reached the level of 6 km. When the mid-sized drops were lofted to mid-levels, they followed the updraft track toward the leading edge and then were slowly sorted out by size toward the front of the convection. Elevated Z_{DR} (>0.5 dB) collocated with low Z_H (<30 dBZ) at heights of 6 km and higher in the forward anvil region of both Figs. 3b and 3d were likely associated with horizontally oriented ice crystals or aggregates of ice crystals.

For the new developing cell in the west of the southern cell, the maximum Z_{DR} reached about 3 dB at the lowest levels corresponding to drops of about 2.8 mm in diameter (Fig. 3d). The location of the maximum Z_{DR} matched the position of maximum low-level updrafts derived from dual-Doppler analysis (Fig. 3c). At the lowest levels, the contours over 1.5 dB had a front-to-rear slope with height corresponding to the backward updraft. However, even with a maximum Z_{DR} of 3 dB, the 1 dB contour only reached to 3 km. This suggests that the large, oblate raindrops immediately fell out because of relatively weak updrafts at low levels. The mid-sized raindrops with Z_{DR} of 0.5-1.0 dB followed a trajectory straight upward between the levels of 3 to 4.5 km. At this developing stage, the mid-sized particles were concentrated only at low levels. Compared to other analysis of tropical MCS, e.g. in Maritime Continent by Carey and Rutledge (2000) and Amazon by Cifelli et al. (2002), the height and magnitude of the Z_{DR} column shown here were quite low. At the onset stage of the SCS summer monsoon, the low-level convergence and updrafts associated with the convection were relatively weak

and not sufficient to lift hydrometeors aloft to sub-freezing temperatures, e.g., to the level of mixed phase. For the case studied here, the low-level inflow had to pass a downdraft and cooled region before entering the updraft. Modified air in the low-level updraft may have reduced the buoyancy and hence updraft speed, contributing further to a low height and magnitude of the Z_{DR} column.

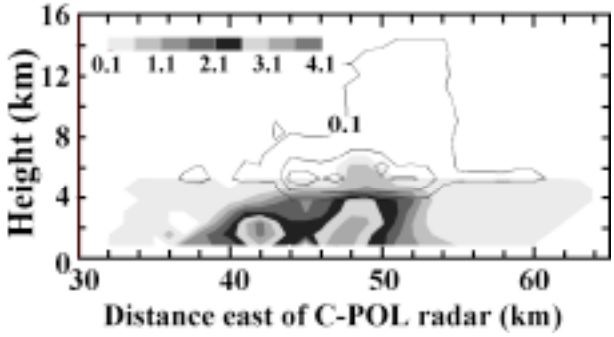

Fig. 4 Vertical cross section of rain water content (g m^{-3}) (shaded), precipitation ice water content (g m^{-3}) (contoured at 0.1, 0.6 and 1.1).

Representative cross-section of rainwater content for the intense southern cell (Fig. 4) exhibited comparable maxima in the developing (e.g., 4 g m^{-3} at 41 km east of C-POL) and mature (e.g., 3.5 g m^{-3} at 49 km east of C-POL) cells at low-levels (2 km MSL). However, analysis of Figs. 3 and 4 reveal that the kinematic and microphysical processes leading to these maxima at different stages of the convective lifecycle were somewhat distinct.

In the developing cell, the maximum water content of over 4 g m^{-3} was located at 1.5-2.5 km MSL above the maximum Z_{DR} at the lowest level. The gentle low-level updrafts allowed sufficient time for the collision-coalescence process to develop both large raindrops and high rainwater contents. However the weak low-level updrafts were unable to lift the largest raindrops found at the lowest level further upward. Those large drops with mean mass-weighted diameter (D_m) of 2.0-3.0 mm were offset below the maximum water content due to size sorting by the updraft. It was the drops with D_m of 1.5-2.0 mm at around 2 km MSL that contributed to the maximum rainwater content in the developing convective core. Given the very weak updrafts at 3-5 km MSL, there was no indication of the lofting of raindrops above the freezing level in the developing convection. As a result, there is very little precipitation ice mass in the developing cell. The lack of significant raindrop freezing also denied the extra buoyancy that is contributed by latent heat release of freezing to the growing cells. This behavior is in stark contrast to tropical continental convection, which typically exhibits vigorous lofting of supercooled raindrops in the strong low-level updrafts, and the initial production of large quantities of precipitation ice mass (i.e., frozen drops) during the developing stage (Carey and Rutledge, 2000; Cifelli et al. 2002). On the other hand, the precipitation structure of the developing cell over the SCS was similar to the maritime-like convection over the "green ocean" of the Amazon during the low-level westerly wind regime (Cifelli et al. 2002).

In the mature cell, the low-level updrafts were still weak, promoting continued warm rain processes, but large raindrops (D_m > 2 mm) had already precipitated out since the updrafts were unable to keep them aloft. As a result, the maximum rainwater content up to 3.5 g m^{-3} was collocated with the maximum Z_{DR} (1.0-1.2 dB or D_m = 1.6-1.8 mm) at the lowest level. Mid-level updrafts were larger in the mature as compared to the developing convection and were capable of lofting a small zone of supercooled rain drops about 1 km above the freezing level (e.g., Fig. 4 at 49 km east of CPOL). Freezing of the supercooled drops caused a slight enhancement in the precipitation ice mass (0.6 to 1.2 g m^{-3}) at mid-levels (5-6.5 km MSL) in the mature cell. However, the vertical extent of the Z_{DR} column (Fig. 7d, 10) was modest and hence supercooled drops and enhanced precipitation ice mass associated with frozen drops were present only in the lowest (or warmest) portions of the mixed-phase zone. As noted before, the mature convection is similar in this regard to the maritime-like convection over the Amazon during the westerly wind regime and very unlike the vigorous tropical continental convection during the easterly regime of the Amazon (Cifelli et al. 2002) and the tropical island convection studied by Carey and Rutledge (2000), which were both characterized by strong and vertically extensive Z_{DR} columns and hail/frozen drop zones. The frozen drops likely fell through the updraft in the mature cell, melted, and hence contributed to the rain water maximum at lower levels. As a result, rain at later stages of convection on 24 May was likely the combination of both warm and modest mixed-phase precipitation processes.

In general, very few raindrops were lofted above the freezing level and precipitation sized ice was scarce on 24 May. Therefore, only those smallest particles were observed at high levels (echo top up to 15 km in Fig. 3c). Due to the dry air at the upper levels, those ice particles might actually evaporate or sublimate and never hit the ground. This also likely explained the lack of stratiform rain on 24 May. By comparison, stratiform rainfall was widespread in the "green ocean" convection over the Amazon during the westerly regime (Cifelli et al. 2002). The key difference appears

to be the relative lack of dry air in the 500-200 hPa layer and hence evaporation/ sublimation during the westerly regime of Amazonian convection (Halverson et al. 2002).

4. COMPOSITE VERTICAL STRUCTURE

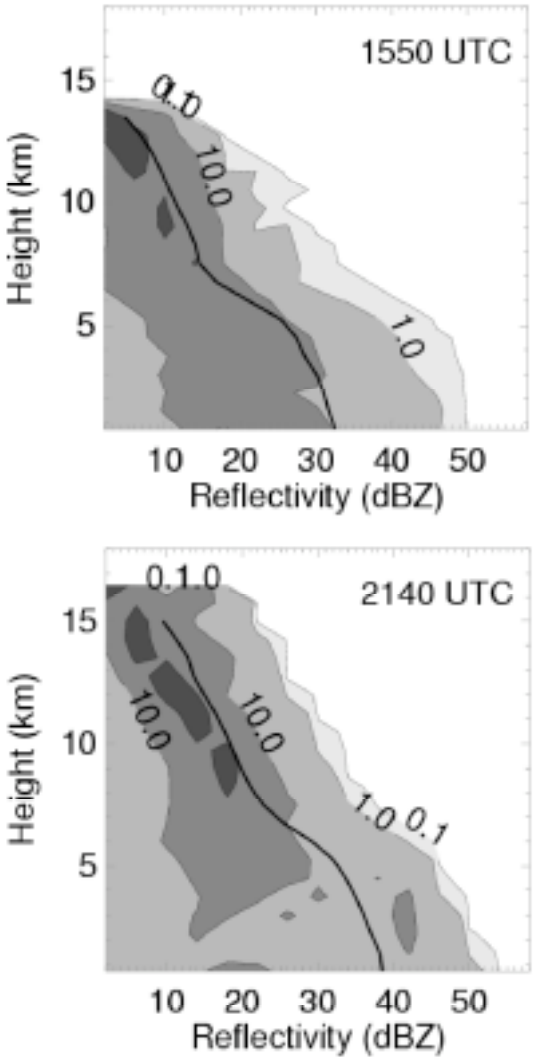

Fig. 5 CFADs and mean profiles of radar reflectivity at 1550 UTC and 2140 UTC, 24 May. Bin size is 4 dBZ.

In this section, mean profiles and contoured frequency by altitude diagrams (CFADs, Yuter and Houze 1995) are used to present statistically characteristics of the squall lines observed on 24 May. The CFAD summarizes frequency distribution information about a variable in a given radar echo volume. It is a convenient tool to display multiple histograms in a two-dimensional format. The relative frequency of occurrence of a given parameter in the area of detectable echo can be shown at each height. Comparison of the reflectivity distribution, system relative winds, and polarimetric measurements with the other subtropical and tropical convection documented in the literature are made to describe the characteristics of the squall line occurring during the late stage of the SCS summer monsoon onset.

The CFADs and mean profiles of reflectivity at 1550 UTC and 2140 UTC, when the first and second squall line reached their peak stage respectively, are shown in Fig. 5. The second squall line was apparently taller and more intense than the first one. The echo top of the second squall line reached 16 km MSL, comparing to 14 km MSL for the first squall line. The mean reflectivity profile at the lowest level was just over 30 dBZ for the first squall line, and near 40 dBZ for the second squall line. Both squall lines had a slowly decreasing mean reflectivity with increasing height near the melting layer. A sharp decrease of mean reflectivity was evident from 5 to 8 km MSL above the melting layer, consistent with the weak updrafts in tropics (Zipser 1977). This decrease was more pronounced at 1550 UTC indicating even weaker updrafts for the first squall line. The decrease of mean reflectivity slowed again in the layers above 8 km MSL. In general, the overall mode of the mean reflectivity profile for both squall lines on 24 May was very similar to the tropical oceanic MCS events summarized by Jorgensen and LeMone (1989) and Zipser and Lutz (1994). At 2-4 km MSL, the occurrence of reflectivity over 40 dBZ, an indicator of intense convection, was over 10% at 2140 UTC, but far less than that frequency at 1550 UTC. At upper levels, the convection at 2140 UTC also had a significantly higher frequency of occurrence of intense echo features. The probability of occurrence of 30 dBZ echo fell below 1% at about 9 km MSL at 2140 UTC compared to 6 km MSL at 1550 UTC. DeMott and Rutledge (1998) suggested that the rainfall production is larger for radar echoes with higher maximum 30 dBZ echo heights. Supporting their argument, our calculation showed that convective rain rates in the first squall line at 1550 UTC were about 55-65 mm hr^{-1}, while rain rates of the convective cores in the second squall line at 2140 UTC reached up to 80-90 mm hr^{-1}.

To examine the statistical kinematic structure of the squall line, we also present the mean profiles and CFAD diagrams of system relative u-component, v-component and divergence at 2040 UTC, when a detailed dual-Doppler analysis was performed for the mature stage of the second squall line, in Fig. 10. The negative u-component dominated at low levels. Since the system moved eastward, this indicated a front to

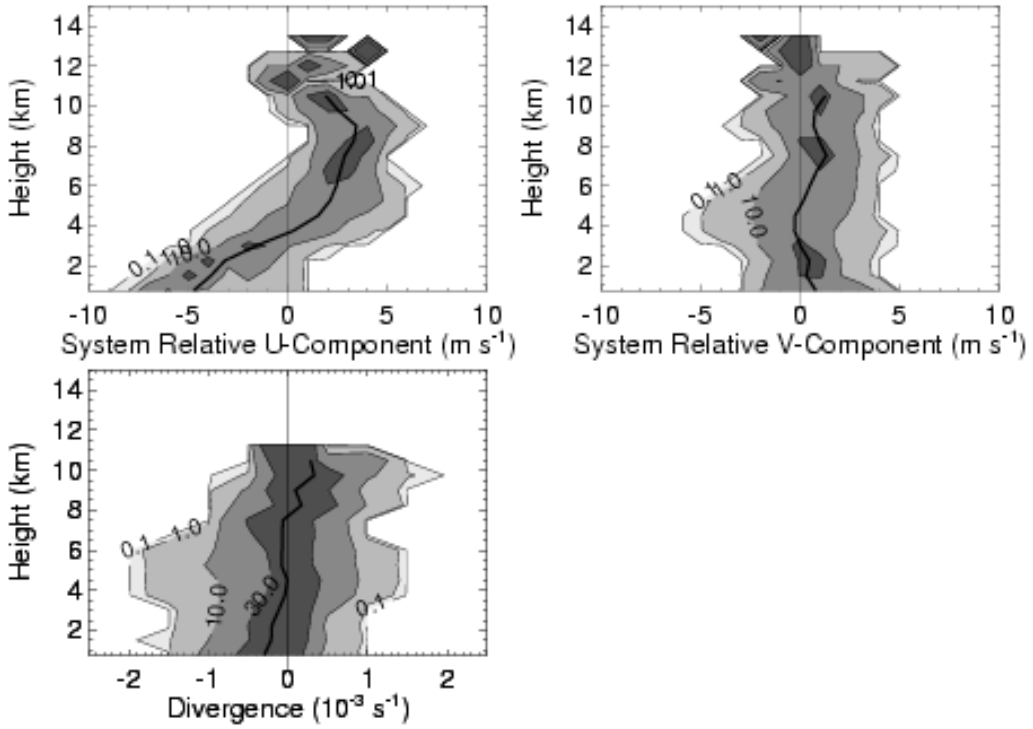

Fig. 6 CFADs and mean profiles of system relative u- and v-component, and divergence at 2040 UTC 24 May. Bin size is 4 dBZ for reflectivity, 1 m s^{-1} for u- and v-component, and 1 $10^{-3}s^{-1}$for divergence.

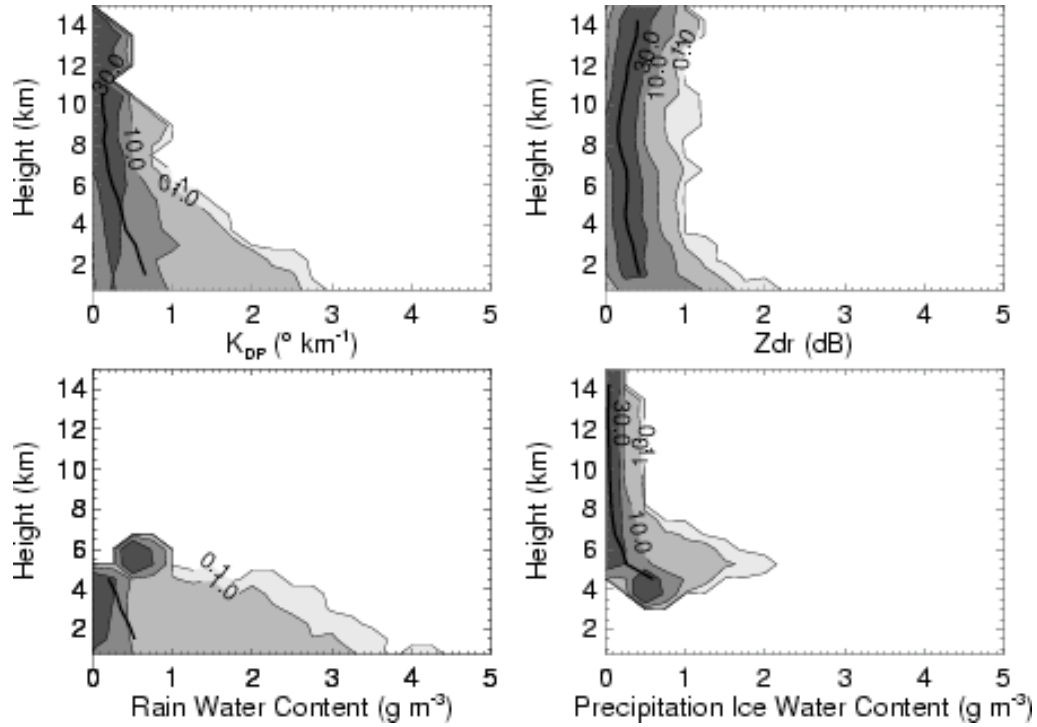

Fig. 7 CFADs and mean profiles of specific differential phase (° km^{-1}), differential reflectivity (dB), rainwater content (g m^{-1}), and precipitation ice water content (g m^{-1}) at 2040 UTC 24 May. Bin size is 0.25 units for all variables.

rear low-level inflow. The mean inflow speed was at 5 m s^{-1} at the lowest level and decreased with the increase of height. The mean profile of u-component turned to be positive at levels above 4 km MSL. The upper-level outflow reached a maximum at about 9 km MSL. The CFAD diagram further supported the observation from vertical cross-section (Fig. 3), i.e., the squall line had an uncommonly strong rear to front outflow. The mean profile of v-component shows a weak system-relative flow along the squall line. The most frequent occurrence (> 30%) of the v-component was near zero or slightly positive. The magnitude of the mean v-component was less than 1.5 m s^{-1} throughout the system. As discussed before, the vertical velocity at higher elevations contained uncertainties when using upward integration as a result of hard define upper boundary condition. Therefore, only the CFAD and mean profile of horizontal winds and divergence field, which are less sensitive to the boundary conditions, are shown. Not surprisingly, the maximum of mean convergence peaked at the lowest level. The magnitude of the convergence decreased gradually until 4 km MSL. Weak convergence existed up to 8 km MSL. This deep layer of convergence implied an elevated maximum vertical velocity at that time.

To compliment the statistical kinematic properties of the squall line above, we present the mean profiles and CFAD diagrams of the specific differential phase, differential reflectivity, rainwater content, and precipitation ice water content at 2040 UTC in Fig. 7. On 24 May 1998, the mean K_{DP} near the surface was approximately 0.7° km^{-1} (Fig. 7a), corresponding to a rain rate (R) of 24 mm h^{-1} (Table 1). This relatively large value of mean rain rate is consistent with a large fraction of convective rainfall and a relatively small area of light, stratiform rain compared to other tropical regimes. The highest frequency (> 30%) of occurrence of K_{DP} near the surface was 0.25° km^{-1} or about 10 mm h^{-1}, again confirming the limited amount of stratiform echo. The 1% frequency line near the surface for K_{DP} (R) was about 2.6° km^{-1} (73 mm h^{-1}). This result is close to that found in rainfall during the westerly regime with more maritime characteristics, which was characterized by a 1% line of about 80 mm h^{-1}, during TRMM-LBA (Carey et al. 2001). On the other hand, the easterly regime during TRMM-LBA with more continental characteristics was characterized by a 1% line of about 100 mm h^{-1}. As expected, the largest values of Z_{DR} occurred well below the height of the 0° C level associated with big raindrops (Fig. 11b). The mean Z_{DR} (D_m) for raindrops near the surface was about 0.5 dB (1.2 mm). The (1%, 0.1%) occurrence line for Z_{DR} and D_m was (1.6 dB, 2.2 dB) and (2.0 mm, 2.4 mm), respectively. Comparable values for (1%, 0.1%) occurrence during the easterly and westerly regime of TRMM-LBA were (2.1 mm, 3.0 mm) and (1.9 mm, 2.5 mm), respectively (Carey et al., 2001).

Of course, precipitation ice and rainwater occurred primarily above and below the melt level at about 5 km MSL, respectively (Figs. 7c,d). Most precipitation rain and ice water contents were below about 0.5 g m^{-3} and 0.3 g m^{-3}, respectively. Note that the anomalies in precipitation content near 5 km are associated with the inability of the polarimetric method to differentiate small raindrops (< 1 mm) from precipitation ice. As a result, it is not possible to detect with confidence very low rain (ice) contents above (below) the height of the 0° C level. The mean and maximum rainwater contents increased with distance below the melt level. Maximum rainwater contents for this case approached 5 g m^{-3}. Comparable values during the easterly (westerly) regime over the Amazon during TRMM-LBA were 10 g m^{-3} (6 g m^{-3}) (Carey et al. 2001, Cifelli et al., 2002). The largest ice water contents (0.5 – 2 g m^{-3}) occurred in the mixed-phase zone between 5 km and 8 km. Similar maximum ice water contents occurred in the westerly regime over the Amazon during TRMM-LBA (Cifelli et al., 2002). On the other hand, maximum ice water contents in the easterly regime over the Amazon were typically from 3-8 g m^{-3} in the mixed phase zone. Consistent with the reflectivity CFAD's above, the frequency of ice water contents in excess of 1 g m^{-3} for this case decreased rapidly from 5 km and 8 km.

Overall, we found that precipitation characteristics inferred from polarimetric radar for this case over the SCS during SCSMEX were similar to the westerly regime over the southwestern Amazon during TRMM-LBA. Both of them had lower rain rates and rainwater contents, smaller raindrops, and significantly lower ice water contents between 5 km and 8 km than the precipitation over the Amazon during the easterly regime of the TRMM-LBA.

5. SUMMARY

In this study, dual-Doppler and polarimetric radar analyses were combined for the first time to study the structure and rainfall characteristics of an oceanic squall line system. Our focus was to link the kinematics of the convective system to the microphysical fields. The similarities and differences of this squall line system occurring in the late SCS summer monsoon onset with tropical and subtropical squall lines observed in previous studies were also discussed.

Compared to the tropical and subtropical oceanic squall lines documented in the literature, the squall lines studies here had significant departures from the archetypal conceptual model. Characterized by

convection with maximum radar reflectivity about 55 dBZ, the squall lines had little stratiform precipitation. The stratiform rain coverage accounted for only 10-15% of total rain area, compared to an overall 63-70% of stratiform occurrence during four TRMM field experiments in the tropics. The dominance of convective echo was likely related to the environmental conditions, i.e., the dry air aloft along with the weak system-relative upper-level winds. For the oceanic squall line case studied herein, the weak vertical velocity and limited buoyancy were not able to generate a strong enough mesoscale circulation to overcome the deleterious microphysical effects of evaporation in a dry environment and further form a large area of stratiform rain. The moistening of the mid-level shown in the sounding taken after the passage of the first squall line confirmed the quick evaporation of hydrometers carried aloft by weak updraft. Meanwhile, the weak environmental winds at the upper level also limited the extension of the possible stratiform rain by failing to advect the hydrometers away from the convective part. From a vertical cross-section, we were able to catch a limited formation of stratiform rain associated with an intense cell from the second squall line. Different from the typical position of the stratiform rain that is usually behind its counterpart, the stratiform rain observed here was ahead of the convective core. It is believed that the relative weak vertical circulation observed in this study could not produce a strong cold pool sufficient to produce an upshear tilted (trailing stratiform) convection. In addition, a pronounced low-level jet, often observed in tropical squall lines, was missing in this case. The absence of the low-level jet removed the reverse shear above the jet and prevented the development of trailing stratiform rain. This type of leading-stratiform mode, although much less frequently observed than trailing-stratiform mode before, occurred quite often during the onset period of SCS summer monsoon.

Differences in the kinematic structure of the squall lines in this study compared to other tropical and subtropical squall lines documented in previous studies may play an important role in deciding the mode of stratiform precipitation. In a typical tropical oceanic squall line, strong low-level convergence and updrafts are found in a narrow zone close to the leading edge where the inflow interacts with the cold pool resulting from evaporation cooling. The new cells form ahead of the old ones. The low-level updrafts then go upward to the rear portion of the system and form stratiform rain there. A large area of downdrafts is often observed behind the convective core. However, for the case of 24 May, the low-level convergence and updrafts were located in a wider convective area in the rear portion of the system. The new cells formed behind the old ones, and the updrafts turned forward like a return flow at the mid-to-upper levels, bringing hydrometers ahead of the convective core. Weak downdrafts ahead of the updrafts were also evident. In addition to the many differences of the squall lines observed on 24 May from previously studied tropical and subtropical oceanic squall lines, some similarities between them are also noteworthy: 1) the low-level inflow from the air ahead of the leading edge, 2) the maximum radar reflectivity at the lowest levels, 3) the gradual decrease of mean reflectivity with height below the melting layer and above 8 km MSL, and 4) the strong mean reflectivity gradient from the 0°C isotherm level to 8 km MSL implying a relatively weak updraft.

The rain and hydrometeor characteristics of the squall line were also examined. The height and magnitude of the differential reflectivity were low compared to the other analyses on tropical MCS. During the early stage of the SCS summer monsoon, the low-level convergence and updrafts were relatively weak and unable to lift the hydrometers to a higher level. In developing cells, the gentle low-level updrafts allowed sufficient time for the collision-coalescence process to develop both large raindrops and high rainwater contents. However the weak low-level updrafts were unable to lift the largest raindrops found at the lowest level further upward. Those large drops were offset below the maximum water content due to size sorting by the updraft. There was no indication of the lofting of raindrops above the freezing level due to weak updrafts in the mid-levels. As a result, there is very little precipitation ice mass in the cell. In the mature cell, the maximum rainwater content was collocated with the maximum Z_{DR} at the lowest level as the large raindrops had already precipitated out because of the weak updrafts. Mid-level updrafts were larger in the mature as compared to the developing convection and were capable of lofting a small zone of supercooled rain drops about 1 km above the freezing level. However, the vertical extent of the Z_{DR} column (Fig. 7d, 10) was modest and hence supercooled drops and enhanced precipitation ice mass associated with frozen drops were present only in the lowest (or warmest) portions of the mixed-phase zone.

From a statistical point of view, compared to the studies focusing on tropical convection observed during the TRMM-LBA experiment, we found that precipitation characteristics of this case over the SCS monsoon region during SCSMEX were similar to the westerly regime over the Amazon monsoon region during TRMM-LBA. However, higher rain rates and rainwater contents, larger raindrops, and significantly higher ice water contents between 5 km and 8 km

defined the precipitation over the Amazon during the easterly regime of the TRMM-LBA.

ACKNOWLEDGEMENTS

This research was sponsored by National Aeronautics and Space Administration (NASA) under TRMM Grants NAG5-9699.

REFERENCES

Carey, L. D., and S. A. Rutledge, 2000: The relationship between precipitation and lightening in tropical island convection: A C-band polarimetric radar study. *Mon. Wea. Rev.*, **128**, 2687-2710.

————, R. Cifelli, W. A. Peterson, S. A. Rutledge, and M. A. F. Silva Dias, 2001: Characteristics of Amazonian rain measured during TRMM-LBA. *30th International Conference on Radar Meteorology*. Preprints, Munich, Germany, Amer. Meteor. Soc., 682-684.

Cifelli, R., W. A. Peterson, L. D. Carey, and S. A. Rutledge, 2002: Radar observation of the kinematic, microphysical, and precipitation characteristics of two MCSs in TRMM-LBA. *J. Geophys. Res.*, 107(D20), 8077, doi:10.1029/2000JD000264.

DeMott, C. A., and S. A. Rutledge, 1998: The vertical structure of TOGA COARE convection. Part I: Radar echo distributions. *J. Atmos. Sci.,* **55**, 2730-2747.

Halverson, J. B., T. Rickenbach, B. Roy, H. Pierce, E. Williams, 2002: Environmental characteristics of convective systems during TRMM-LBA. *Mon. Wea. Rev.*, **130,** 1493–1509.

Houze, R. A., Jr., 1993: *Cloud Dynamics*. Academic Press, 573pp.

Johnson, R. H. and P. E. Ciesielski, 2002: Characteristics of the 1998 summer monsoon onset over the northern South China Sea. *J. Meteor. Soc. Japan*, **80**, 561-578.

Jorgensen, D. P., and M. A. LeMone, 1989: Vertical velocity characteristics of oceanic convection. *J. Atmos. Sci.,* **46**, 621-640.

————, and ————, and S. B. Trier, 1997: Structure and evolution of the 22 February 1993 TOGA COARE squall line: aircraft observations of precipitation, circulation, and surface energy fluxes. *J. Atmos. Sci.,* **54**, 1961-1985.

Lau, K.-M., Y. Ding, J.-T. Wang, R. Johnson, T. Keenan, R. Cifelli, J. Gerlach, O. Thiele, T. Rickenbach, S. C. Tsay, and P.-H. Lin, 2000: Report of the field operations and early results of the South China Sea Monsoon Experiment (SCSMEX). *Bull. Amer. Meteor. Soc.*, **81**, 1261-1270.

LeMone, M. A., G. M. Barnes, E. J. Szoke, and E. J. Zipser, 1984: The tilt of the leading edge of mesoscale tropical convective lines. *Mon. Wea. Rev.*, **112**, 510-519.

————, E. J. Zipser, and S. B. Trier, 1998: The role of environmental shear and thermodynamic conditions in determining the structure and evolution of mesoscale convective systems during TOGA COARE. *J. Atmos. Sci.,* **55**, 3493-3518.

Parker, M. D., 2002: Dynamics of convective lines with leading precipitation. *21st Conference on Severe Local Storms.* Preprints, San Antonio, TX, Amer. Meteor. Soc., 5-8.

————, and R. H. Johnson, 2000: Organizational modes of midlatitude mesoscale convective systems. *Mon. Wea. Rev.*, **128**, 3413-3436.

Robe, F. R. and K. A. Emmanuel, 2001: The effect of vertical wind shear on radiative–convective equilibrium states. *J. Atmos. Sci.,* **58**, 1427–1445.

Rotunno, R., J. B. Klemp, and M. L. Weisman, 1988: A theory for strong, long-lived squall line. *J. Atmos. Sci.,* **45**, 463-485.

Roux, F., 1988: The West African squall line observed on 23 June 1981 during COPT 81: Kinematics and thermodynamics of the convective region. *J. Atmos. Sci.,* **45**, 406–426.

Simpson, J. (Ed.), 1988: TRMM: *A Satellite Mission to Measure Tropical Rainfall, Report of the Science Steering Group*. National Aeronautics and Space Administration, Goddard Space Flight Center, Greenbelt, Maryland 20771, 94pp.

Steiner, M., R. A. Houze Jr., S. E. Yuter, 1995: Climatological characteristics of three-dimensional storm structure from operational radar and rain gauge data. *J. Appl. Meteorol.,* **34**, 1978–2007.

Tao, W.-K., C.-L. Shie, J. Simpson, S. Braun, R. H. Johnson, P. E. Ciesielski, 2003: Convective systems over the South China Sea: cloud-resolving model simulations. *J. Atmos. Sci.,* **60**, 2929–2956

Tokay, A., R. Meneghini, J. Kwiatkowski, E. Amitai, T. Kuzu, T. Iguchi, C. Williams, M Kulie, and C. Wilson, 2001: On the role of drop size distribution in TRMM rain profiling Algorithm. *30th International Conference on Radar Meteorology*. Preprints, Munich, Germany, Amer. Meteor. Soc., 345-347.

Trier, S. B., W. C. Skamarock, M. A. LeMone, D. B. Parsons, and D. P. Jorgensen, 1996: Structure and evolution of the 22 February 1993 TOGA COARE squall line: Numerical simulations. *J. Atmos. Sci.,* **53**, 2861-2886.

———, W. C. Skamarock, M. A. LeMone, 1997: Structure and evolution of the 22 February 1993 TOGA COARE squall line: organization mechanisms inferred from numerical simulation. . *J. Atmos. Sci.,* **54,** 386–407.

Wang, J.-J., 2004: Evolution and structure of the mesoscale convection and its environment: A case study during the early onset of south east Asian summer monsoon. *Mon. Wea. Rev.*, **132**, 1104-1120.

Yuter, S. E., and R. A. Houze Jr., 1995: Three-dimensional kinematic and microphysical evolution of Florida cumulonimbus. Part II: Frequency distributions of vertical velocity, reflectivity, and differential reflectivity. *Mon. Wea. Rev.*, **123**, 1941-1963.

Zipser, E. J., 1977: Mesoscale and convective-scale downdrafts as distinct components of squall-line structure. *Mon. Wea. Rev.*, **105**, 1568-1589.

———, and M. A. LeMone, 1980: Cumulonimbus vertical velocity events in GATE. Part II: Synthesis and model core structure. *J. Atmos. Sci.,* **37**, 2458-2469.

———, and K. Lutz, 1994: The vertical profile of radar reflectivity of convective cells: A strong indicator of storm intensity and lightning probability? *Mon. Wea. Rev.*, **122**, 1751-1759.